

Lasing with Topological Weyl Semimetal

Güneş Oktay,^{1,*} Mustafa Sarısan,^{1,†} and Murat Tas^{2,‡}

¹*Department of Physics, Istanbul University, 34134, Vezneciler, Istanbul, Turkey*

²*Department of Software Engineering, Altınbaş University, 34217 Istanbul, Turkey*

Lasing behavior of optically active planar topological Weyl semimetal (TWS) is investigated in view of Kerr and Faraday rotations. Robust topological character of TWS is revealed by the presence of Weyl nodes and relevant surface conductivities. We focus our attention on the surfaces where no fermi arcs are formed, and thus Maxwell equations contain topological terms. We explicitly demonstrate that two distinct lasing modes arise because of the presence of effective refractive indices which lead to the birefringence phenomena. Transfer matrix is constructed in such a way that reflection and transmission amplitudes involve 2×2 matrix-valued components describing the bimodal character of the TWS laser. We provide associated parameters of the laser system yielding the optimal impacts. Our proposal is supported by the corresponding graphical demonstrations. Our observations and predictions suggest a concrete way of forming TWS laser and coherent perfect absorber and are awaited to be confirmed by an experimental realization based on our computations.

PACS numbers: 03.65.Nk, 24.30.Gd, 42.25.Bs, 42.60.Da, 68.65.Pq, 71.55.Ak

INTRODUCTION

Introducing mathematical ideas into the physical theories is one of the special moments of theoretical physics, which always arouses a great enthusiasm. Incorporating topology in the material science caused an emergence of a new and impressive field of physics, topological materials [1, 2]. Especially, their photonics application researches carried the flag one step ahead in view of the researches in the field of topological photonics [3, 4]. Recently, constructing a theoretical modeling of topological insulator lasers and their experimental realization attracted attention to this field [5, 6]. Motivated by these recent findings, we build up a theoretical modeling of a topological Weyl semimetal (TWS) laser in this paper.

TWS, one of leading candidates of topological materials, has attracted much attention in recent years for its novel gapless band structure in the bulk and exotic Fermi arcs on the surface states. Theoretical predictions of this exclusive phase of topological materials has been made since 2011 [7–11], and the first experimental verification of this phase was reported in TaAs material in 2015 [12, 13]. Recently, great interest in the TWS phase has arisen from the possibility of realization of this phase in certain condensed matter systems. There are various predictions of solid materials as potential TWS candidates [14–16], although their energy structures and topological properties are not perfectly consistent with an ideal TWS. In fact, an ideal TWS proposed in [14] is rare in nature, and makes the analysis of the corresponding properties of TWS, i.e. the spin texture of the boundary states, the flat bands, and the transport properties, quite difficult [17, 18]. Their interaction with electromagnetic waves is thus quite intriguing, and gives rise to substantial applications of them, especially in developing new photonics devices. In this study, we fulfill

a comprehensive treatment of electromagnetic scattering of these attractive materials just to unveil their lasing features and corresponding CPA applications.

An optically active laser system can be obtained by means of the existence of spectral singularities [19–21]. Hence, we mount a homogeneous gain environment in a planar TWS slab such that TWS properties are preserved in a way that corresponding Weyl nodes are not affected, and fermi arcs are present on its surfaces. Once electromagnetic waves are incident on a surface which does not contain a fermi arc, polarization directions of the reflected and transmitted waves change due to Kerr and Faraday rotations on the surfaces. This leads to the modified Maxwell equations involving topological terms in source parts. Solution of these equations reveals coupled Helmholtz equations whose solutions yield a 4×4 transfer matrix. We show that the form of transfer matrix provides a basis for the bimodal laser. This is characteristics of a TWS laser system such that purely outgoing waves cause rotated output intensity due to Kerr and Faraday rotations. A coherent perfect absorber (CPA) using TWS can be thus obtained by adjusting appropriate polarizations given by Faraday rotations together with the exact phase and amplitude modulations [22–25]. This happens by virtue of the fact that CPA has the time reversal symmetry of a laser.

Although our problem is one dimensional, Kerr and Faraday rotations take the problem into two-dimensional plane, see Fig. 1. Therefore, reflection and transmission amplitudes are expressed by 2×2 matrices. Dimension of these matrices decides bimodal structure of TWS laser system. Spectral singularities for each mode are established by the divergent characteristics of reflection and transmission matrices. Hence, we obtain uni- or bimodal spectral singularity conditions with/without dispersion effects. We look for practical ways to improve the ef-

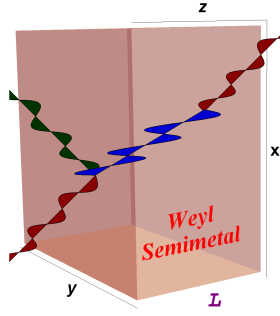


FIG. 1: (Color online) Figure displays the TE mode configuration for the interaction of electromagnetic wave with the Weyl semimetal slab system. Wave is emitted on the slab system by an angle θ which is measured from the normal to the surface, and the direction of polarization is rotated by an angle of θ_F and θ_K inside and outside of the slab respectively.

efficiency of laser and CPA systems through the supplemented material features. It is noted that our formalism is satisfied by all TWS type materials.

We find complete solutions, schematically demonstrate their behaviors and deduce the effects of various parameter choices yielding laser conditions in the framework that we develop. We reveal the optimal control of parameters in a TWS uni- or bimodal slab laser, which include gain coefficient, incidence angle, slab thickness and Weyl node separation. These optimal parameters give rise to a desired outcome of achieving rotated outgoing waves in the uni- or bimodal TWS laser system. We also present the way to find exact conditions causing the achievement of TWS CPA with equal amplitude and phase values of ingoing waves which are obtained by adjusting correct Faraday rotation angles. Our method, and thus results guide possible experimental studies in this direction for all proposed TWS slab materials of practical concern.

TE MODE SOLUTION AND TRANSFER MATRIX

Consider a linear homogeneous and optically active gain slab system which is made up of a TWS material whose Weyl nodes are aligned along the z -axis as depicted in Fig. 1. The slab is designed in such a way that it has a thickness L and a complex refractive index \mathbf{n} which is uniform between the end-faces of the slab in the region $0 < z < L$. Interaction of this TWS optical slab system with the electromagnetic waves requires an elaborate analysis of the properties of TWS in view of topological and magnetoelectric optical effects. Topological features is crucial based on the alignment of Weyl nodes which specify the locations of fermi arcs on the faces of the slab. In our set-up, fermi arcs appear on the side faces of the slab along the z -direction since Weyl nodes

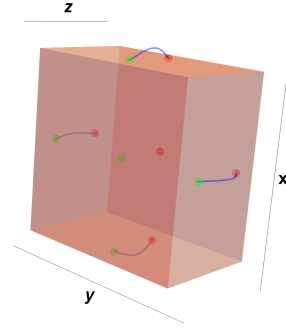


FIG. 2: (Color online) Figure depicts the schematic representation of the locations of Weyl nodes along k_z -axis in bulk Brillouin zone, which are the sources (green dot) and sinks (pink dot) of Berry curvature. Fermi arcs corresponding to Weyl nodes are formed on the relevant surfaces.

are oriented in z -axis as shown in Fig. 2. In light of this optical setup, Maxwell's equations turn out to include topological terms (see Appendix A for the derivation of the topological terms) which are shown to take the form of

$$\begin{aligned}\vec{\nabla} \cdot \vec{\mathcal{D}} &= \rho(z) + \beta \vec{b} \cdot \vec{\mathcal{B}}, & \vec{\nabla} \cdot \vec{\mathcal{B}} &= 0, \\ \vec{\nabla} \times \vec{\mathcal{H}} - \partial_t \vec{\mathcal{D}} &= \vec{\mathcal{J}}(z) - \beta \vec{b} \times \vec{\mathcal{E}}, & \partial_t \vec{\mathcal{B}} + \vec{\nabla} \times \vec{\mathcal{E}} &= \vec{0}.\end{aligned}\quad (1)$$

Here $\beta := 2\alpha/\pi Z_0$ is a constant, $\alpha := e^2/4\pi\epsilon_0\hbar c$ is the fine structure constant, $Z_0 := \sqrt{\mu_0/\epsilon_0}$ is the vacuum impedance, e is the charge of an electron and $c := 1/\sqrt{\epsilon_0\mu_0}$ is the speed of light in vacuum. The vector notation \vec{b} specifies the distance between two Weyl nodes which are aligned in z -direction and is given explicitly by $\vec{b}(z) = b(z)\hat{e}_z$, and $b(z) = bu(z)u(L-z)$, where $u(z)$ is the Heaviside step function which is defined by

$$u(z) := \begin{cases} 0 & \text{for } z < 0 \\ 1 & \text{for } z > 0 \end{cases}$$

Notice that $\vec{\mathcal{E}}$ and $\vec{\mathcal{B}}$ represent the electric and magnetic fields respectively, and are expressed by $\vec{\mathcal{D}}$ and $\vec{\mathcal{H}}$ fields via the following constitutive relations

$$\vec{\mathcal{D}} := \tilde{\epsilon} \vec{\mathcal{E}}, \quad \vec{\mathcal{B}} := \tilde{\mu} \vec{\mathcal{H}},$$

where $\tilde{\epsilon}$ and $\tilde{\mu}$ are respectively permittivity and permeability of the relevant environment in which electromagnetic wave propagates. These are described by $\tilde{\epsilon} := \epsilon_0\epsilon$ and $\tilde{\mu} := \mu_0\mu$ respectively in terms of vacuum permittivity and permeability, where we defined

$$\epsilon(z) := \begin{cases} \epsilon_b + \frac{i\sigma_{yy}}{\epsilon_0\omega} & \text{for } z \in [0, L], \\ 1 & \text{otherwise} \end{cases} \quad (3)$$

$$\mu(z) := \begin{cases} 1 + \chi_m & \text{for } z \in [0, L], \\ 1 & \text{otherwise} \end{cases} \quad (4)$$

ε_b is the bound charge contribution, χ_m is the magnetic susceptibility of TWS provided that it exhibits a magnetic characteristics. In this paper, we assume that TWS is endowed with a rather weak magnetism such that we may ignore it [45]. Notice that $\mathbf{n}^2 := \varepsilon\mu$ within the slab according to the expressions (3) and (4), where \mathbf{n} corresponds to the complex-valued refractive index of TWS, and is described by real and imaginary parts as follows

$$\mathbf{n} := \eta + i\kappa \quad (5)$$

We observe that free charges and currents in our optical setup appear only on surfaces of the TWS slab on which the incident wave emerges and no fermi arcs are present. This is because of the topological character of TWS which leads to form conductivities only on the surfaces whereas it behaves as an insulator inside the TWS medium. Therefore, surface charge density $\rho^s(z)$ and conductivity $\sigma^s(z)$ can be written as

$$\begin{aligned} \rho^s(z) &:= \rho^{(1)}\delta(z) + \rho^{(2)}\delta(z-L), \\ \sigma^s(z) &:= \sigma^{(1)}\delta(z) + \sigma^{(2)}\delta(z-L), \end{aligned}$$

where $\rho^{(j)}$ and $\sigma^{(j)}$ are respectively the free charge and conductivity on the j -th layer, with $j = 1, 2$. Notice that $\rho^s(z)$ and $\sigma^s(z)$ are associated to each other by the continuity equation

$$\vec{\nabla} \cdot \vec{\mathcal{J}}^s + \partial_t \rho^s(z) = 0 \quad (6)$$

for the electric current density given by $\vec{\mathcal{J}}^s := \sigma^s(z)\vec{\mathcal{E}}$. Surface conductivity σ^s has a tensorial expression and thus we can demonstrate the surface current $\vec{\mathcal{J}}^s$ as $\vec{\mathcal{J}}^s = \sigma_{\alpha\beta}^s \vec{E}_\beta$. In our case,

$$\sigma_{yy}^s = \frac{e^2 k_c}{3\pi h \hat{\omega}_c} \{1 - i[\hat{\omega}_c^2 + \ln|1 - \hat{\omega}_c^2|]\} \quad (7)$$

$$\sigma_{yx}^s = \frac{e^2 b}{\pi h} + \frac{\alpha c}{3\pi v_F} \ln|1 - \hat{\omega}_c^2| \quad (8)$$

where $\hat{\omega}_c := 2\omega_c/\omega$, $\omega_c := v_F k_c$, v_F is the Fermi velocity, k_c is the momentum cut-off and $k \leq k_c$, see Appendix for the details of the derivations of (7) and (8). We emphasize that the conductivity σ_{yx}^s is responsible for the Kerr and Faraday rotations inside and outside the TWS. Consider time harmonic electromagnetic waves [46] having TE mode solutions corresponding to our geometrical design such that electromagnetic wave can be regarded as obliquely incident in the form, see Fig. 1

$$\vec{E}(\vec{r}) = \mathcal{E}(z)e^{ik_x x} \hat{e}_y, \quad (9)$$

In this notation, \hat{e}_j denotes the unit vector along the j -axis, with $j = x, y$ and z , and k_j is the component of wavevector \vec{k} in the j -direction, where \vec{k} is given by

$$\vec{k} = k_x \hat{e}_x + k_z \hat{e}_z$$

such that $k_x = k \sin\theta$, $k_z = k \cos\theta$ and $\theta \in [-90^\circ, 90^\circ]$ represents the incident angle. We notice that polarization direction of the emitted wave will be twisted once it is reflected and refracted at the interface of TWS. Reflected waves give rise to Kerr rotation while the refracted waves to Faraday rotation within the slab, see Fig. 1.

Maxwell equations in (1) and (2) can be manipulated to give 3-dimensional Helmholtz equation associated with the TE mode states and the corresponding magnetic field \vec{H} as follows

$$[\nabla^2 + k^2 \varepsilon(z)\mu(z)] \vec{E} - i\beta k Z_0 \vec{b} \times \vec{E} = 0, \quad (10)$$

$$\vec{H} = -\frac{i}{k Z_0 \mu(z)} \vec{\nabla} \times \vec{E}, \quad (11)$$

TE mode solution [47] of (10) in view of Kerr and Faraday rotations can be established by means of the following one-dimensional coupled Helmholtz equations

$$\mathcal{E}_x'' + k_z^2 \mathfrak{z}(z) \mathcal{E}_x + i\beta k Z_0 b \mathcal{E}_y = 0 \quad (12)$$

$$\mathcal{E}_y'' + k_z^2 \mathfrak{z}(z) \mathcal{E}_y - i\beta k Z_0 b \mathcal{E}_x = 0 \quad (13)$$

where a prime denotes derivative with respect to z and the piecewise constant function $\mathfrak{z}(z)$ is specified by

$$\begin{aligned} \mathfrak{z}(z) &:= \begin{cases} \tilde{\mathbf{n}}^2 & \text{for } z \in [0, L], \\ 1 & \text{otherwise} \end{cases} \\ \tilde{\mathbf{n}} &:= \sec\theta \sqrt{\mathbf{n}^2 - \sin^2\theta} \end{aligned}$$

We next introduce the following scaled variables for the convenience of subsequent expressions

$$\mathbf{x} := \frac{x}{L}, \quad \mathbf{z} := \frac{z}{L}, \quad \mathfrak{K} := Lk_z = kL \cos\theta. \quad (14)$$

Solutions of (12) and (13) are attained once we split them in uncoupled modes as follows

$$\psi_\pm(\mathbf{z}) := \mathcal{E}_x(L\mathbf{z}) \pm i\mathcal{E}_y(L\mathbf{z})$$

where ψ_\pm are the solutions of Schrödinger equations

$$-\psi_\pm'' + v_\pm(\mathbf{z})\psi_\pm = \mathfrak{K}^2 \psi_\pm \quad (15)$$

for the potentials given by $v_\pm(\mathbf{z}) = \mathfrak{K}^2 \mathfrak{z}_\pm(\mathbf{z})$. Here $\mathfrak{z}_\pm(\mathbf{z})$ is defined as

$$\mathfrak{z}_\pm(\mathbf{z}) := \mathfrak{z}(\mathbf{z}) \pm \frac{2\alpha L b(\mathbf{z})}{\pi \mathfrak{K} \cos\theta} \quad (16)$$

Notice that refractive indices $\tilde{\mathbf{n}}_\pm = \sqrt{\mathbf{n}^2 \pm 2\alpha b L / \pi \mathfrak{K} \cos\theta}$ within the TWS slab lead to the birefringence effect because of the presence of uncoupled modes in (16). In view of (11), (15) and (16), one finds components of the electric field \vec{E} and magnetic field \vec{H} as in Table I, where the quantities \mathcal{F}_\pm and \mathcal{G}_\pm are defined in different regions of optical TWS slab system by

$$\mathcal{F}_\pm := \begin{cases} A_1^{(-)} e^{i\mathfrak{K}\mathbf{z}} \pm C_1^{(-)} e^{-i\mathfrak{K}\mathbf{z}} & \text{for } \mathbf{z} < 0, \\ B_1^{(+)} e^{i\mathfrak{K}\mathbf{z}} \pm B_2^{(+)} e^{-i\mathfrak{K}\mathbf{z}} & \text{for } 0 < \mathbf{z} < 1, \\ A_1^{(+)} e^{i\mathfrak{K}\mathbf{z}} \pm C_1^{(+)} e^{-i\mathfrak{K}\mathbf{z}} & \text{for } \mathbf{z} > 1. \end{cases}$$

Components of \vec{E} -field	Components of \vec{H} -field
$E_x = \frac{(\mathcal{F}_+ + \mathcal{G}_+)}{2} e^{i\mathfrak{R}\mathbf{x} \tan \theta}$	$H_x = \frac{i \cos \theta}{2Z_0} [\sqrt{\mathfrak{z}_+} \mathcal{F}_- - \sqrt{\mathfrak{z}_-} \mathcal{G}_-] e^{i\mathfrak{R}\mathbf{x} \tan \theta}$
$E_y = \frac{-i(\mathcal{F}_+ - \mathcal{G}_+)}{2} e^{i\mathfrak{R}\mathbf{x} \tan \theta}$	$H_y = \frac{\cos \theta}{2Z_0 \mu} [\sqrt{\mathfrak{z}_+} \mathcal{F}_- + \sqrt{\mathfrak{z}_-} \mathcal{G}_-] e^{i\mathfrak{R}\mathbf{x} \tan \theta}$
$E_z = 0$	$H_z = -\frac{i \sin \theta}{2Z_0} [\mathcal{F}_+ - \mathcal{G}_+] e^{i\mathfrak{R}\mathbf{x} \tan \theta}$

TABLE I: Components of \vec{E} and \vec{H} fields existing inside and outside the TWS slab.

$$\mathcal{G}_\pm := \begin{cases} A_2^{(-)} e^{i\mathfrak{R}\mathbf{z}} \pm C_2^{(-)} e^{-i\mathfrak{R}\mathbf{z}} & \text{for } \mathbf{z} < 0, \\ B_1^{(-)} e^{i\mathfrak{R}-\mathbf{z}} \pm B_2^{(-)} e^{-i\mathfrak{R}-\mathbf{z}} & \text{for } 0 < \mathbf{z} < 1, \\ A_2^{(+)} e^{i\mathfrak{R}\mathbf{z}} \pm C_2^{(+)} e^{-i\mathfrak{R}\mathbf{z}} & \text{for } \mathbf{z} > 1. \end{cases}$$

Here we introduced the quantity \mathfrak{K}_j as follows

$$\mathfrak{K}_j := \mathfrak{K} \tilde{\mathbf{n}}_j. \quad (17)$$

The complex coefficients $A_j^{(\pm)}$, $B_j^{(\pm)}$ and $C_j^{(\pm)}$ are possibly \mathfrak{K} -dependent, and related to each other by means of standard boundary conditions. Appropriate boundary conditions in our configuration of the optical system are described by the fact that tangential components of \vec{E} -fields and normal components of \vec{B} -fields are continuous across the interfaces while tangential components of \vec{H} -fields are discontinuous by an amount equal to the surface current density $\vec{\mathcal{J}}$ which is expressed by the conductivities on the corresponding surfaces. See Appendix for the associated boundary conditions. Therefore, transfer matrix following from boundary conditions are obtained as follows

$$\begin{pmatrix} \mathbf{A}^{(+)} \\ \mathbf{C}^{(+)} \end{pmatrix} = \mathbb{M}(\mathfrak{K}) \begin{pmatrix} \mathbf{A}^{(-)} \\ \mathbf{C}^{(-)} \end{pmatrix},$$

where $\mathbf{A}^{(\pm)}$ and $\mathbf{C}^{(\pm)}$ are the column matrices which represent the coefficients of right and left moving waves outside the TWS slab, and are given by

$$\mathbf{A}^{(\pm)} = \begin{pmatrix} A_1^{(\pm)} \\ A_2^{(\pm)} \end{pmatrix}, \quad \mathbf{C}^{(\pm)} = \begin{pmatrix} C_1^{(\pm)} \\ C_2^{(\pm)} \end{pmatrix},$$

and $\mathbb{M}(\mathfrak{K})$ is the 4×4 transfer matrix [42] which is expressed by

$$\mathbb{M}(\mathfrak{K}) = \begin{pmatrix} \mathbf{T}^l - \mathbf{R}^l \mathbf{R}^r \mathbf{T}^{-r} & \mathbf{R}^r \mathbf{T}^{-r} \\ -\mathbf{R}^l \mathbf{T}^{-r} & \mathbf{T}^{-r} \end{pmatrix} \quad (18)$$

Once we impose the reciprocity principle, we understand that $\mathbf{T}^l = \mathbf{T}^r = \mathbf{T}$. Notice that transfer matrix (18) gives rise to deduce all information about the lasing properties of TWS optical configuration since it contains valuable information about reflection and transmission amplitudes. Lasing threshold condition is then given by the spectral singularity expression which is given by the requirement $\mathbb{M}_{22} = 0$ corresponding to the real \mathfrak{K} values. Thus, transmission and right/left reflection amplitudes

are divergent at spectral singularity points. In our TWS configuration, \mathbb{M}_{22} is obtained as follows

$$\mathbb{M}_{22} = \mathbf{T}^{-1} = - \begin{pmatrix} \zeta_-(\nu_+; \nu_-) & \gamma_-(\nu_+; \nu_-) \\ \gamma_-(\nu_-; \nu_+) & \zeta_-(\nu_-; \nu_+) \end{pmatrix} e^{i\mathfrak{K}}, \quad (19)$$

where $\nu_j := (\sigma_j, \tilde{\mathbf{n}}_j)$, and $\zeta_j, \gamma_j : \mathbb{C} \rightarrow \mathbb{C}$ are continuous functions and specified by

$$\begin{aligned} \zeta_j(\nu_+; \nu_-) &:= \frac{1}{2} \left\{ (\sigma_+ - \sigma_- + 2j) \cos \mathfrak{K}_+ - \frac{i\mu\sigma_+^2}{\tilde{\mathbf{n}}_-} \sin \mathfrak{K}_- \right. \\ &\quad \left. + \frac{i[\tilde{\mathbf{n}}_+^2 - \mu^2(\sigma_+ + j)(\sigma_- - j)]}{\mu\tilde{\mathbf{n}}_+} \sin \mathfrak{K}_+ \right\}, \\ \gamma_j(\nu_+; \nu_-) &:= \frac{1}{2} \left\{ \sigma_+ \cos \mathfrak{K}_- + \frac{i\mu\sigma_+(\sigma_- - 1)}{\tilde{\mathbf{n}}_-} \sin \mathfrak{K}_- \right. \\ &\quad \left. - \sigma_- \cos \mathfrak{K}_+ + \frac{i\mu\sigma_-(\sigma_- - j)}{\tilde{\mathbf{n}}_+} \sin \mathfrak{K}_+ \right\}, \end{aligned}$$

with the appropriate identification of σ_j

$$\sigma_j := \frac{\mu_0 \omega L}{2\mathfrak{K}} (\sigma_{yy} + ij\sigma_{yx}) = \frac{Z_0}{2 \cos \theta} (\sigma_{yy} + ij\sigma_{yx}) \quad (20)$$

where $j = +$ or $-$ is implied. Thus, lasing threshold condition of TWS is obtained by means of spectral singularities which are found by the real values of \mathfrak{K} such that matrix components of \mathbb{M}_{22} in Eq. 19 are set to zero. In view of this fact, we realize that each of plus (“+”) and minus (“-”) modes corresponding to the plus/minus refractive indices may lead to form distinctive lasing conditions. This two-mode lasing arises due to the coupling behaviors of solutions appearing in TWS configurations, which is seen by virtue of Kerr and Faraday rotations. Therefore, plus/minus mode lasing is attained by the condition

$$\zeta_-(\nu_\pm; \nu_\mp) = \gamma_-(\nu_\pm; \nu_\mp) = 0. \quad (21)$$

This in turn implies the conditions $A_1^{(-)} = A_2^{(-)} = C_1^{(+)} = 0$ for plus-mode and $A_1^{(+)} = A_2^{(+)} = C_2^{(-)} = 0$ for minus-mode lasing to generate purely outgoing waves. Bimodal-lasing is provided once all four conditions in (21) are imposed. Notice that plus-mode lasing yields lasing in both sides of the slab due to the effective refractive index $\tilde{\mathbf{n}}_+$ and a lasing from left-hand side due to $\tilde{\mathbf{n}}_-$. Likewise, minus-mode lasing leads to a bidirectional lasing from $\tilde{\mathbf{n}}_-$ and a left side lasing due to $\tilde{\mathbf{n}}_+$. This reveals the distinctive character of TWS laser slab. Fig. 3 clearly demonstrates these lasing behaviors of plus and minus-modes.

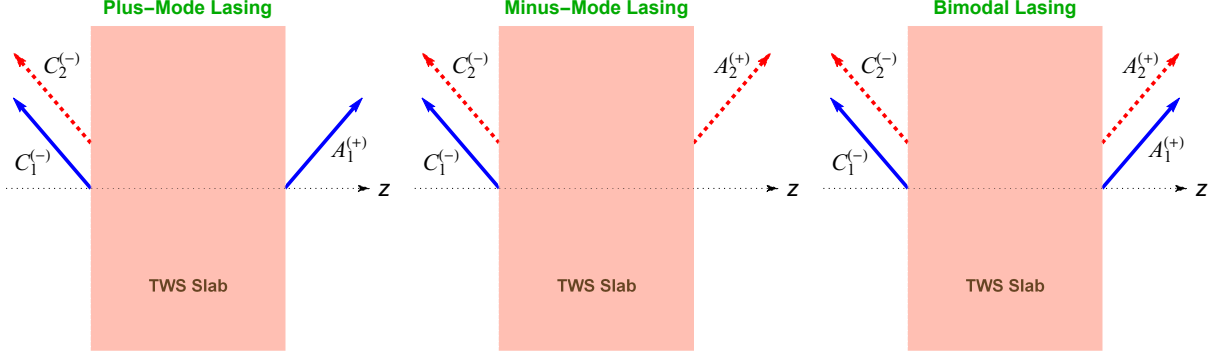


FIG. 3: (Color online) Configurations of uni- and bimodal lasing. Blue solid arrows correspond to lasing due to \tilde{n}_+ and red dashed arrows correspond to lasing due to \tilde{n}_- .

LASING CONDITIONS IN PLUS/MINUS-MODES AND RELATED PARAMETERS

Uni- or bimodal lasing behavior of TWS slab described by Eq. 21 can be further analyzed to reveal conditions for the necessary parameters of the corresponding optical system. An immediate and simultaneous computation of two equations in (21) gives rise to the following expression for each individual mode

$$e^{2i\tilde{\kappa}_j} = -U_j + \sqrt{U_j^2 + 1} \quad (22)$$

with the following identifications

$$U_j := \frac{\mathcal{X}_j \mathcal{Z}_j - \mathcal{Y}_j \sqrt{\mathcal{X}_j^2 - \mathcal{Y}_j^2 + \mathcal{Z}_j^2}}{\mathcal{Y}_j^2 - \mathcal{Z}_j^2}$$

$$\mathcal{X}_j := \frac{1}{2} \{ \mathcal{A}_{2j}^2 - \mathcal{A}_{1j}^2 + \sigma_j^2 [\mathcal{A}_{3j}^2 - \mathcal{A}_{4j}^2 - \mathcal{A}_{5j}^2] \}$$

$$\mathcal{Y}_j := \frac{1}{2} \{ \mathcal{A}_{2j}^2 + \mathcal{A}_{1j}^2 - \sigma_j^2 [\mathcal{A}_{3j}^2 + \mathcal{A}_{4j}^2] \}$$

$$\mathcal{Z}_j := \mathcal{A}_{1j} \mathcal{A}_{2j} + \sigma_j^2 \mathcal{A}_{3j} \mathcal{A}_{4j}$$

$$\mathcal{A}_{1j} := \sigma_j - \sigma_{-j} - 2, \quad \mathcal{A}_{2j} := \frac{\tilde{n}_j^2 - \mu^2 (\sigma_j - 1) (\sigma_{-j} + 1)}{\mu \tilde{n}_j}$$

$$\mathcal{A}_{3j} := \frac{\mu}{\tilde{n}_{-j}} [(\sigma_{-j} - 1) (\sigma_+ - \sigma_- + 1 - 2j) + 1]$$

$$\mathcal{A}_{4j} := \frac{\mu^2 (\sigma_{-j} + 1) [(\sigma_{-j} - 1) \mathfrak{a}_j + 1] - j (\sigma_{-j} - 1) \tilde{n}_j^2}{\tilde{n}_- \tilde{n}_+},$$

$$\mathcal{A}_{5j} := \frac{\sqrt{2} \mu}{\tilde{n}_{-j}}, \quad \mathfrak{a}_j := 1 + j (\sigma_j - 1),$$

where the subindex $j = +$ and $-$ corresponds to the plus and minus modes. Uni- or bimodal lasing behavior of our TWS system is controlled by the expression (22). We realize that surface conductivities σ_j associated with each mode are the manifestation of bimodal lasing attitude, which stems from the presence of Weyl nodes and

thus the Kerr and Faraday rotations. If the conditions of forming TWS is removed or disturbed considerably, the condition of uni- or bimodal lasing in Eq. 22 is violated. Notice that (22) is a complex expression which displays the behavior of system parameters of our optical setup. The most appropriate system parameters should be chosen for the emergence of optimal impacts. Thus, it can be explored extensively by means of relevant physical quantities containing significant consequences by splitting into the real and imaginary parts. In this direction, refractive index of TWS described by Eq. 5 leads to the effective refractive indices which are bifurcated as follows

$$\tilde{n}_j \approx \tilde{\eta}_j + i\tilde{\kappa}_j, \quad (23)$$

with the identifications

$$\tilde{\eta}_j := \sec \theta \sqrt{\eta^2 - \sin^2 \theta + \frac{2j\alpha b L \cos \theta}{\pi \mathfrak{K}}}, \quad \tilde{\kappa}_j := \frac{\eta \kappa \sec^2 \theta}{\tilde{\eta}_j}.$$

Notice that expression for \tilde{n}_j in Eq. 23 makes use of the condition that most of the materials including TWS satisfy

$$|\kappa| \ll \eta - 1 < \eta.$$

Next we introduce the gain coefficient g by

$$g := -2k\kappa = -\frac{4\pi\kappa}{\lambda} = -\frac{2\mathfrak{K}\kappa}{L \cos \theta}. \quad (24)$$

Therefore, uni- or bimodal spectral singularity condition expressed by Eq. 22 gives rise to the following expressions for gain coefficient g_j and effective wavenumber \mathfrak{K}^j [48]

$$g_j = \frac{\tilde{\eta}_j \cos \theta}{2\eta L} \ln |\mathcal{V}_j|, \quad (25)$$

$$\mathfrak{K}^j = \frac{1}{2\tilde{\eta}_j} \sin^{-1} \left\{ \frac{-\text{Im}[\mathcal{U}_j] + \sqrt{\mathcal{W}_j} \sin\left(\frac{\Phi_j}{2}\right)}{\sqrt{\mathcal{V}_j}} \right\}, \quad (26)$$

where we define the associated quantities

$$\begin{aligned}\mathcal{V}_j &:= \mathcal{W}_j + \text{Re}[\mathcal{U}_j]^2 + \text{Im}[\mathcal{U}_j]^2 \\ &\mp 2\sqrt{\mathcal{W}_j} \left[\sin\left(\frac{\Phi_j}{2}\right) \text{Im}[\mathcal{U}_j] + \cos\left(\frac{\Phi_j}{2}\right) \text{Re}[\mathcal{U}_j] \right], \\ \mathcal{W}_j &:= \sqrt{\text{Re}[\mathcal{U}_j]^4 + (\text{Im}[\mathcal{U}_j]^2 - 1)^2 + 2\text{Re}[\mathcal{U}_j]^2(\text{Im}[\mathcal{U}_j]^2 + 1)}, \\ \Phi_j &:= \tan^{-1} \left\{ \frac{2\text{Re}[\mathcal{U}_j]\text{Im}[\mathcal{U}_j]}{1 + \text{Re}[\mathcal{U}_j]^2 - \text{Im}[\mathcal{U}_j]^2} \right\},\end{aligned}$$

and Re and Im correspond to the real and imaginary part of the relevant quantity, respectively. We explore the most appropriate system parameters through the expressions of gain coefficient g_j and \mathfrak{R}^j in Eqs. 25 and 26 for the emergence of optimal impacts. Thus, a comprehensive analysis of the involvement of system parameters is required to observe the final outcome. For this purpose we exhibit the general behaviors of system parameters through the physically applicable gain coefficient g plots. But, notice that g_- -value in (25) does not allow lasing for some wavelength configurations due to the presence of the parameter $\tilde{\eta}_-$. Although it is not explicitly seen in the expression for g_+ , the same restriction holds for g_+ as well. This in turn implies that distance b between Weyl nodes in Brillouin zone must satisfy

$$b < \frac{\pi^2(\eta^2 - \sin^2\theta)}{\alpha\lambda}. \quad (27)$$

In position space, this corresponds to

$$b' > \frac{2\alpha\lambda}{\pi(\eta^2 - \sin^2\theta)}, \quad (28)$$

if we introduce $b := 2\pi/b'$. In (28), the lower bound of b' can be identified by $b'_c := 2\alpha\lambda/\pi(\eta^2 - \sin^2\theta)$. Thus we realize that the lower bound of b' depends on the incidence angle θ and wavelength λ . But θ has little effect compared to λ . Therefore, once the wavelength is increased, the corresponding b'_c value is reduced in order to observe a lasing in both plus and minus modes. The following graphs display the justification of our calculations which are based on the following specifications of a nonmagnetic ($\mu \approx 1$) TaAs TWS slab system [27–31]

$$\begin{aligned}\eta &\approx 6, & \lambda &= 1400 \text{ nm}, & L &= 1 \text{ cm}, \\ \theta &= 30^\circ & \text{and} & & b' &= 0.05 \text{ \AA}.\end{aligned} \quad (29)$$

Fig. 4 reveals the effect of Weyl node separation b' in position space on the gain coefficient g for the realization of lasing. Gain values are tightly packed. Notice that both plus and minus nodes give rise to a minimal bound b'_c , below which no lasing occurs. The best lasing impact with high quality factor is acquired by opting a TWS material whose Weyl node separation is around the critical b' -value. b'_c -value raises slightly by increasing the incidence angle θ , and significantly by the wavelength rise.

Fig. 5 shows how b'_c varies with respect to wavelength λ and incidence angle θ .

Thickness of TWS slab plays a rather distinctive role in case of lasing. The thicker TWS slab is, the higher quality factor is achieved. This is obviously seen in Fig. 6. We realize that the less gain is obtained once we choose a relatively small wavelength λ and incidence angle θ . As we increase λ and θ , the required gain values of plus and minus modes increase and also differ considerably.

Finally, Fig. 7 displays the dependence of incidence angle on gain coefficient g to achieve lasing. Notice the compact patterns that occur in both plus and minus modes. Again minus mode arises at small gain values compared to the plus mode. One can easily obtain the bimodal lasing using these patterns by observing the overlapping positions of plus and minus modes. For instance, Fig. 8 shows one such a case for a TWS system with parameters of incident angles $\theta \approx 3.42''$ and $\theta \approx 3.46''$ at gain value $g \approx 1.17 \times 10^{-9} \text{ cm}^{-1}$.

EFFECT OF DISPERSION

If there exists a dispersion in refractive index \mathbf{n} , then we need to consider the effect of wavenumber k on \mathbf{n} . We imagine that active part of the TWS optical system with the gain ingredient is formed by doping a host medium of refractive index n_0 and its refractive index satisfies the dispersion relation

$$\mathbf{n}^2 = n_0^2 - \frac{\hat{\omega}_p^2}{\hat{\omega}^2 - 1 + i\hat{\gamma}\hat{\omega}}, \quad (30)$$

where $\hat{\omega} := \omega/\omega_0$, $\hat{\gamma} := \gamma/\omega_0$, $\hat{\omega}_p := \omega_p/\omega_0$, ω_0 is the resonance frequency, γ is the damping coefficient, and ω_p is the plasma frequency. $\hat{\omega}_p^2$ can be described in the leading order of the imaginary part κ_0 of \mathbf{n} at the resonance wavelength $\lambda_0 := 2\pi c/\omega_0$ by the expression $\hat{\omega}_p^2 = 2n_0\hat{\gamma}\kappa_0$, where quadratic and higher order terms in κ_0 are ignored, [26]. We replace this equation in (30), employ (5) and neglecting quadratic and higher order terms in κ_0 , we obtain the real and imaginary parts of refractive index as follows [22, 26]

$$\eta \approx n_0 + \frac{\kappa_0\hat{\gamma}(1 - \hat{\omega}^2)}{(1 - \hat{\omega}^2)^2 + \hat{\gamma}^2\hat{\omega}^2}, \kappa \approx \frac{\kappa_0\hat{\gamma}^2\hat{\omega}}{(1 - \hat{\omega}^2)^2 + \hat{\gamma}^2\hat{\omega}^2} \quad (31)$$

κ_0 can be written as $\kappa_0 = -\lambda_0 g_0/4\pi$ at resonance wavelength λ_0 . Substituting this relation in (31) and making use of (5) and (22), we can determine the λ and g_0 values for the uni- or bimodal TWS laser. In our optical configuration, TWS slab material holds the following values of the parameters refractive index, resonance wavelength and the corresponding $\hat{\gamma}$ value [27, 29–31]:

$$\begin{aligned}n_0 &= 6, & \lambda_0 &= 1378 \text{ nm}, & \hat{\gamma} &= 0.033, \\ \theta &= 30^\circ, & L &= 1 \text{ cm}.\end{aligned} \quad (32)$$

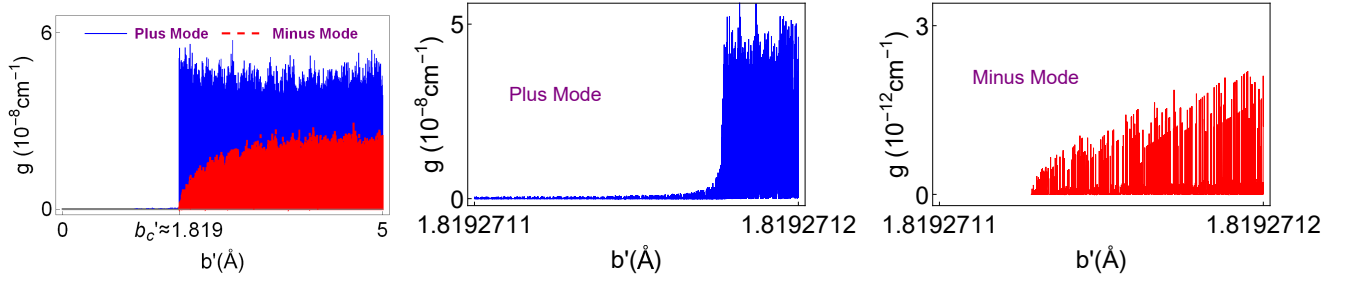


FIG. 4: (Color online) Gain coefficient as a function of Weyl node separation b' corresponding to plus and minus modes for the configuration of the TWS slab system given in (29). Here, b'_c denotes the critical b' value which corresponds to the minimum b' -value that allows lasing. Last two Figs. indicate the region that b'_c takes effect. Horizontal gray line matches up to the zero gain limit.

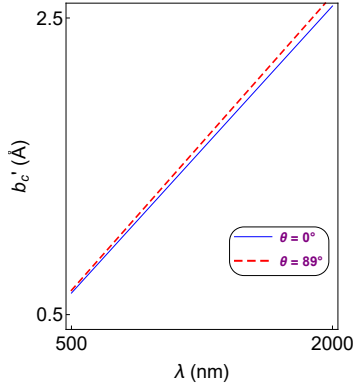


FIG. 5: (Color online) Dependence of critical b'_c -value on the wavelength λ for various incidence angles, corresponding to both plus and minus-mode lasing.

Spectral singularity points which give rise to the lasing threshold conditions are explicitly calculated for various parameters in Table II for our setup of the TWS slab in (32). Fig. 9 displays the positions of lasing points in $\lambda - g_0$ plane, which yield divergent quality factors. It is apparent that wavelength layout corresponding to the each particular mode is incompatible with the reciprocal mode unless they do coincide, in which case a bimodal lasing occurs. In our case, $\lambda \approx 1378.0735$ nm is the wavelength for the bimodal lasing. It is remarkable to realize that only particular discrete wavelengths allow lasing whereas threshold gain values are rather small compared to regular optical slab materials. This is encountered only with a TWS slab laser.

KERR AND FARADAY ROTATIONS IN LASING AND CPA

We now turn our attention to the discussion of Kerr and Faraday rotations which need to be understood to unveil the lasing behaviors and characteristics inside and

κ	g_0 (cm $^{-1}$)	λ (nm)	Type of Lasing
-1.800×10^{-13}	1.6419×10^{-8}	1377.997	Plus Mode
-6.341×10^{-14}	5.7827×10^{-9}	1378.0278	Plus Mode
-1.539×10^{-13}	1.4031×10^{-8}	1378.0586	Plus Mode
-4.089×10^{-14}	3.7286×10^{-9}	1377.9909	Minus Mode
-1.238×10^{-13}	1.1287×10^{-8}	1378.0320	Minus Mode
-1.927×10^{-14}	1.7572×10^{-9}	1378.0594	Minus Mode
-1.237×10^{-13}	1.1280×10^{-8}	1378.0735	Bimodal
-6.554×10^{-14}	5.9773×10^{-9}	1378.0735	Bimodal

TABLE II: Types and corresponding configurations of a TWS slab laser with $L = 1$ cm and $\theta = 30^\circ$.

outside the TWS slab, and explicitly see their impressive features. Since lasing is structured by spectral singularities, we impose the spectral singularity conditions given in (21) or (22), and then impose the conditions $A_1^{(-)} = A_2^{(-)} = C_1^{(+)} = 0$ for plus-mode and $A_1^{(+)} = A_2^{(+)} = C_2^{(-)} = 0$ for minus-mode lasing to obtain the necessary configurations of electric fields inside and outside the TWS slab, see [23] for details of this calculation. When we attain the spectrally singular fields, we can easily construct spectrally singular right and left circularly polarized fields $E_{\pm}(\mathbf{z})$, which are given by

$$E_+(\mathbf{z}) = \mathcal{F}_+(\mathbf{z}) e^{i\mathbf{R}\mathbf{x} \tan \theta}, \quad E_-(\mathbf{z}) = \mathcal{G}_+(\mathbf{z}) e^{i\mathbf{R}\mathbf{x} \tan \theta}.$$

Therefore, Kerr and Faraday rotation angles are determined to be $\theta_K := (\arg E_+(\mathbf{z}) - \arg E_-(\mathbf{z}))/2$ for $\mathbf{z} \notin [0, 1]$ and $\theta_F := (\arg E_+(\mathbf{z}) - \arg E_-(\mathbf{z}))/2$ for $\mathbf{z} \in [0, 1]$ respectively, where \arg refers to the argument of corresponding quantity. Notice that when $\mathbf{z} < 0$ or $\mathbf{z} > 1$ we find Kerr rotation angles θ_K which are equal in magnitude due to reciprocal response of the system. This observation leads to an important consequence about CPA lasers built by TWS systems. Necessary and sufficient condition to generate a TWS CPA laser is to emit waves from both sides using polarizations exactly at Faraday angle θ_F with the appropriate phases and magni-

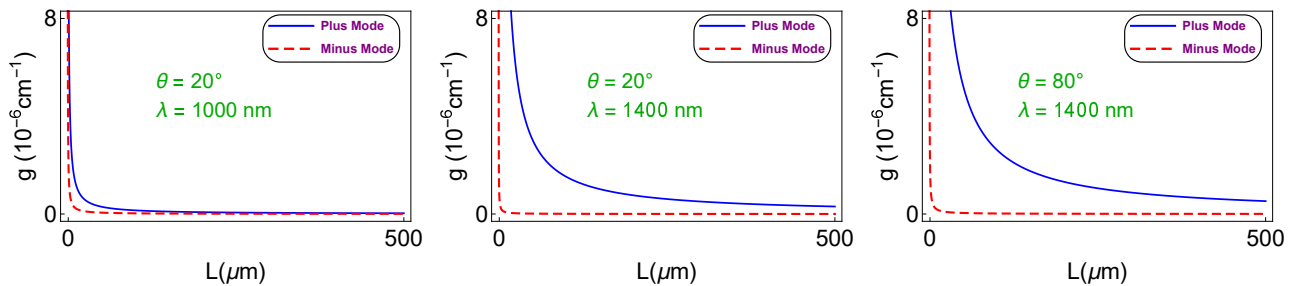


FIG. 6: (Color online) Gain coefficient as a function of TWS slab thickness L corresponding to various incidence angles and wavelengths. Increasing incidence angle and wavelength lead to higher gain values, and favor plus mode.

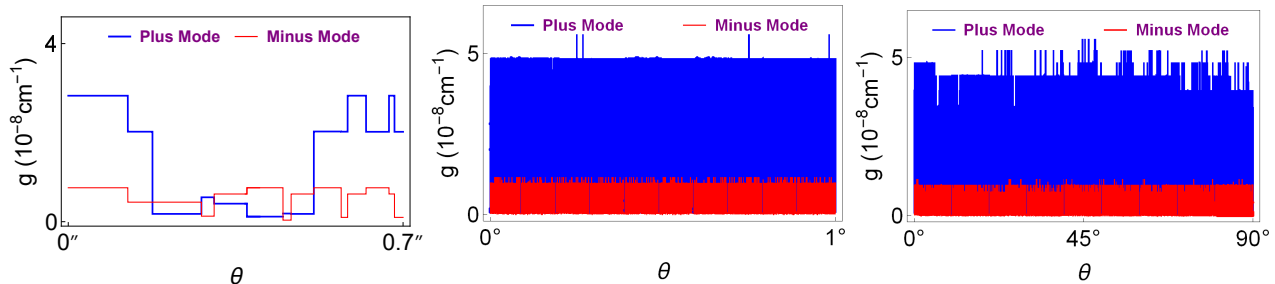


FIG. 7: (Color online) Gain coefficient as a function of incident angle θ . Here the symbol $''$ simply refers to the Arcsecond, which is given by $1'' = 1^\circ/3600$. Notice that patterns are tightly packed once the range of angle is increased.

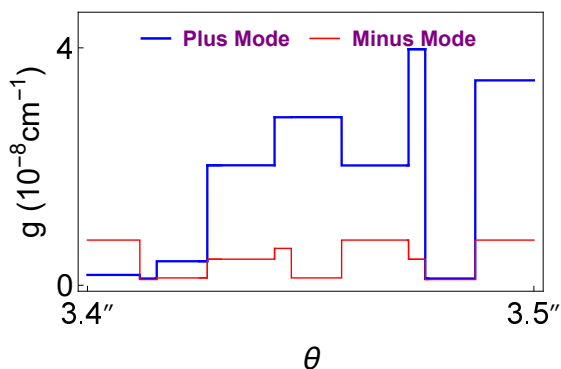


FIG. 8: (Color online) Schematic diagram of gain g as a function of incident angle θ for plus and minus lasing modes. Plus and minus modes overlap at angles $\theta \approx 3.42''$ and $\theta \approx 3.46''$ at the gain value $g \approx 1.17 \times 10^{-9} \text{ cm}^{-1}$.

tudes [23–25]. This is due to the main idea of a CPA that is time reversal symmetry of a regular laser [34–41]. Since this procedure requires special attention with excessive efforts, we reserve it for another study in its own right.

CONCLUDING REMARKS

In this study, we reveal basics of constructing a TWS laser by means of transfer matrix approach. We employ the known features of TWS such that presence of Weyl nodes gives rise to appear Fermi arcs on relevant surfaces to exist magneto-optical effects. Alignment of Weyl nodes determines how these magneto-optical effects response to the scattering of TWS slab. If the electromagnetic waves fall on the surface which has Fermi arcs, Maxwell equations turn out to be in simple familiar form, and do not contain any topological terms. Besides, interesting case occurs when the electromagnetic waves are exposed to the surface with no Fermi arcs, which is what we have explored in the present paper. This case induces Maxwell equations with topological terms which give rise to coupled Helmholtz equations. We observed that this coupling refers to the inherent feature of Kerr and Faraday rotations of a generic TWS slab.

Our discussion strongly embraces the transfer matrix method such that boundary conditions are highly effective [22, 42–44]. Since the basic characteristics of a TWS slab manifest itself by the effects of surfaces, this method becomes notable in this respect. We find out the transfer matrix, and obtained the condition of spectral singularities which lead to construct a TWS slab laser. We notice that our one dimensional problem turns into a two dimensional one by virtue of Kerr and Faraday rotations.

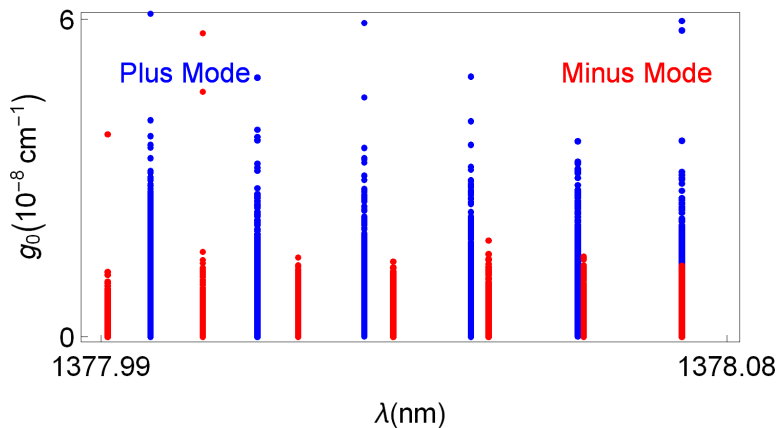


FIG. 9: (Color online) The threshold gain g_0 as a function of wavelength λ corresponding to both plus and minus modes. Plus mode is represented by blue dots while minus modes by red ones. Overlapping dots which take place at wavelength $\lambda \approx 1378.0735$ nm imply the bimodal positions.

This gives a bimodal laser system corresponding to effective refractive indices \tilde{n}_{\pm} in (16), which generate lasing in plus and minus modes as discussed in (22). These distinctive modes are peculiar to a TWS laser system, which can also be observed in any material with magneto-optical effects. We find out that exact lasing modes of a TWS slab are provided by the spectral singularity condition in (21). In particular, plus mode lasing provides bidirectional lasing due to \tilde{n}_{+} and left-side lasing due to \tilde{n}_{-} , whereas minus mode lasing yields bidirectional one due to \tilde{n}_{-} and left-side lasing due to \tilde{n}_{+} , see Fig. 3.

Lasing characteristics of these modes are obtained by the optimal control of system parameters. We have seen that required gain value for a minus mode lasing is always less than the one for a plus mode. Also relatively smaller TWS slab thickness is sufficient for the minus mode lasing. It is revealed that incident angles corresponding to uni- or bimodal lasing is so sensitive to tiny variations, and depends on adjusting definite gain value. For some distinct angles with appropriate gain values, one can obtain bimodal lasing as seen in Fig. 8. This remarkable feature is explicitly seen in case of dispersion effect in Fig. 9 such that only some specific wavelengths give rise to bimodal lasing. Once all other parameters are fixed, uni- or bimodal lasing occurs only at discrete wavelengths. Moreover, increasing wavelength gives rise to higher Weyl node separations as in Fig. 4 when the remaining parameters are fixed. Considering all these behaviors of parameters, one can construct a highly effective TWS slab laser. We present some samples of these optimal parameters in Table II.

A CPA laser can also be constructed using a TWS slab. For the realization of a TWS CPA, one needs to adjust appropriate configuration of the whole optical setup because all incoming waves have to be absorbed inside the slab. For this to occur, we replace gain by

the loss, employ exact phase and magnitudes of the incoming waves, and finally set the polarization angle to Faraday rotation angle which can be computed with the help of spectral singularity condition. Because of the arrangement of Faraday rotation angle, a TWS CPA could be challenging. Our findings figure out this problem. We expect the results of this paper to guide experimental attempts for the realization of a concrete TWS laser and CPA.

Appendix

A. Modified Maxwell Equations

In low energy limit of a TWS, spatially varying axion term plays a significant role in determining its electromagnetic response. The full action of corresponding TWS slab system is described by the sum of conventional and axionic terms as $S = S_0 + S_{\Theta}$

$$S_0 = \int \left\{ -\frac{1}{4\mu_0} F_{\mu\nu} F^{\mu\nu} + \frac{1}{2} F_{\mu\nu} \mathcal{P}^{\mu\nu} - J^{\mu} A_{\mu} \right\} d^3x dt,$$

$$S_{\Theta} = \frac{\alpha}{8\pi\mu_0} \int \left\{ \Theta(\vec{r}, t) \varepsilon^{\mu\nu\alpha\beta} F_{\mu\nu} F_{\alpha\beta} \right\} d^3x dt,$$

where $\mathcal{P}^{\mu\nu}$ tensor represents the electric polarization and magnetization respectively by $\mathcal{P}^{0i} = cP^i$ and $\mathcal{P}^{ij} = -\varepsilon^{ijk} M_k$. Space and time dependent axion term is given by $\Theta(\vec{r}, t) = 2\vec{b} \cdot \vec{r} - 2b_0 t$, where \vec{b} and b_0 denote the separation of nodes in momentum and energy space respectively. In our case, b_0 is set to zero, since Weyl nodes are assumed to share the same chemical potential. If the action is varied with respect to A_{μ} , the following equa-

tions of motion is obtained

$$-\frac{1}{\mu_0}\partial_\nu F^{\mu\nu} + \partial_\nu \mathcal{P}^{\mu\nu} + \frac{\alpha}{2\pi\mu_0}\varepsilon^{\mu\nu\alpha\beta}\partial_\nu(\Theta F_{\alpha\beta}) = J^\mu \quad (33)$$

It is obvious that expanding this equation yields the modified Maxwell equations given by Eqs. 1 and 2 in the presence of axion field term.

B. Computation of Conductivities

To calculate the longitudinal σ_{yy} and transverse σ_{yx} conductivities of a TWS, we adopt the approaches given in [32, 33]. We consider the simplest case with only two nodes located at $+\vec{b}$ and $-\vec{b}$, where $\vec{b} = b\hat{e}_z$. Near the Weyl nodes, linearized Hamiltonian is given by

$$H(\vec{k}) = \pm\hbar v_F \vec{\sigma} \cdot (\vec{k} \pm \vec{b}).$$

where v_F is the Fermi velocity, and $\vec{\sigma} = (\sigma_x, \sigma_y, \sigma_z)$ is the vector whose components are Pauli matrices. Therefore, conductivity $\sigma_{\alpha\beta}$ is obtained from Kubo formula as follows

$$\sigma_{\alpha\beta}(\omega) = \frac{i}{\omega} \lim_{q \rightarrow 0} \Pi_{\alpha\beta}(q, \omega)$$

In the absence of diamagnetic term, the polarization function $\Pi_{\alpha\beta}(q, \omega)$ is given by the current-current correlation function

$$\Pi_{\alpha\beta}(q, i\omega_n) = \frac{-1}{\mathcal{V}} \int_0^\beta d\tau e^{i\omega_n\tau} \langle T_\tau \hat{\mathcal{J}}_\alpha(q, \tau) | \hat{\mathcal{J}}_\beta(-q, 0) \rangle.$$

where \mathcal{V} is the volume of the system, and the current density operator $\hat{\mathcal{J}}$ is given by

$$\hat{\mathcal{J}} = -\frac{\delta H}{\delta \vec{A}} = \pm e v_F \vec{\sigma}.$$

Once we make the analytic continuation $i\omega_n \rightarrow \omega + i0^+$, the real frequency behavior is obtained easily. Thus, for each node we obtain

$$\Pi_{\alpha\beta}(\omega) = \frac{e^2 v_F^2}{\mathcal{V}} \sum_{i, i', \vec{k}} \frac{f(\varepsilon_{i'}(\vec{k})) - f(\varepsilon_i(\vec{k}))}{\hbar\omega + \varepsilon_{i'}(\vec{k}) - \varepsilon_i(\vec{k}) + i0^+} \langle \vec{k}i | \sigma_\alpha | \vec{k}i' \rangle \langle \vec{k}i' | \sigma_\beta | \vec{k}i \rangle$$

where $f(x) = 1/(1 + e^{\beta x})$ is the Fermi function. The expression $H(\vec{k}) | \vec{k}i \rangle = \varepsilon_i(\vec{k}) | \vec{k}i \rangle$ with $i = 1, 2$ gives the quasiparticle energies and eigenstates. We can evaluate the longitudinal and transverse polarizations $\Pi_{\alpha\beta}(\omega)$ when Fermi energy lies with nodes. Thus, in low frequency limit, longitudinal and transverse conductivities from both nodes are found to be expressions given in (7) and (8).

C. Boundary Conditions

Boundary conditions across the surface \mathcal{S} between two regions of space are given by the statements: 1) Tangential component of electric field \vec{E} is continuous across the interface, $\hat{n} \times (\vec{E}_1 - \vec{E}_2) = 0$; 2) Normal component of magnetic field vector \vec{B} is continuous, $\hat{n} \cdot (\vec{B}_1 - \vec{B}_2) = 0$; 3) Normal component of electric flux density vector \vec{D} is discontinuous by an amount equal to the surface current density, $\hat{n} \cdot (\vec{D}_1 - \vec{D}_2) = \rho^s$; 4) Tangential component of the field \vec{H} is discontinuous by an amount equal to the surface current density, $\hat{n} \times (\vec{H}_1 - \vec{H}_2) = \vec{J}^s$. Here \hat{n} represents the unit normal vector to the surface \mathcal{S} from region 2 to region 1. In our optical configuration, we do not have the third condition since there is no normal component of electric field. Therefore, we obtain the boundary conditions as in Table III, In this table, we used $\mathfrak{K} := k_z L$ and $\mathfrak{K}_j := \mathfrak{K} \hat{n}_j$. g_j and h_j are defined as follows for convenience

$$g_j := \begin{cases} + & \text{for } j = 1, \\ - & \text{for } j = 2 \end{cases} \quad h_j := \begin{cases} \sigma_+ & \text{for } j = 1, \\ -\sigma_- & \text{for } j = 2 \end{cases} \quad (34)$$

where σ_\pm is specified by Eq. 20.

* Electronic address: gunes.oktay73@hotmail.com

† Electronic address: mustafa.sarisaman@istanbul.edu.tr

‡ Electronic address: murat.tas1@altinbas.edu.tr, tasm236@gmail.com

- [1] B. Yan and S. C. Zhang, Rep. Prog. Phys. **75**, 096501 (2012).
- [2] B. Yan and C. Felser, Annu. Rev. Condens. Matter Phys. **8**, 337-354 (2017).
- [3] A. B. Khanikaev, S. H. Mousavi, W. K. Tse, M. Kargarian, A. H. MacDonald, and G. Shvets, Nature Materials **12**, 233-239 (2013).
- [4] T. Ozawa, H. M. Price, A. Amo, N. Goldman, M. Hafezi, L. Lu, M. Rechtsman, D. Schuster, J. Simon, O. Zeitler, I. Carusotto, Rev. Mod. Phys. **91**, 015006 (2019).
- [5] G. Harari, M. A. Bandres, Y. Lumer, M. C. Rechtsman, Y. D. Chong, M. Khajavikhan, D. N. Christodoulides, M. Segev, Science **359**, 1230 (2018).
- [6] M. A. Bandres, S. Wittek, G. Harari, M. Parto, J. Ren, M. Segev, D. N. Christodoulides, M. Khajavikhan, Science **359**, 1231 (2018).
- [7] X. -G. Wan, A. M. Turner, A. Vishwanath, and S. Y. Savrasov, Phys. Rev. B **83**, 205101 (2011).
- [8] G. Xu, H. Weng, Z. Wang, X. Dai, and Z. Fang, Phys. Rev. Lett. **107**, 186806 (2011).
- [9] A. A. Burkov and L. Balents, Phys. Rev. Lett. **107**, 127205 (2011).
- [10] L. Lu, L. Fu, J. D. Joannopoulos, and M. Soljačić, Nat. Photon. **7**, 294 (2013).
- [11] S. -M. Huang, S. -Y. Xu, I. Belopolski, C. -C. Lee, G. Chang, B. Wang, N. Alidoust, G. Bian, M. Neupane, C. Zhang, S. Jia, A. Bansil, H. Lin, and M. Z. Hasan, Nat. Commun. **6**, 7373 (2014).

$$\begin{aligned}
& \sum_{j=1}^2 [A_j^{(-)} + C_j^{(-)}] = \sum_{j=-}^+ [B_1^{(j)} + B_2^{(j)}], \\
& \sum_{j=1}^2 g_j [A_j^{(-)} + C_j^{(-)}] = \sum_{j=-}^+ j [B_1^{(j)} + B_2^{(j)}], \\
\mathbf{z} = 0 & \quad \mu \sum_{j=1}^2 [(g_j + 2h_j) A_j^{(-)} - (g_j - 2h_j) C_j^{(-)}] = \sum_{j=-}^+ j \tilde{n}_j [B_1^{(j)} - B_2^{(j)}], \\
& \quad \mu \sum_{j=1}^2 [A_j^{(-)} - C_j^{(-)}] = \sum_{j=-}^+ \tilde{n}_j [B_1^{(j)} - B_2^{(j)}]. \\
\hline
& \sum_{j=1}^2 [A_j^{(+)} e^{i\tilde{\mathbf{R}}} + C_j^{(+)} e^{-i\tilde{\mathbf{R}}}] = \sum_{j=-}^+ [B_1^{(j)} e^{i\tilde{\mathbf{R}}_j} + B_2^{(j)} e^{-i\tilde{\mathbf{R}}_j}], \\
& \sum_{j=1}^2 g_j [A_j^{(+)} e^{i\tilde{\mathbf{R}}} + C_j^{(+)} e^{-i\tilde{\mathbf{R}}}] = \sum_{j=-}^+ j [B_1^{(j)} e^{i\tilde{\mathbf{R}}_j} + B_2^{(j)} e^{-i\tilde{\mathbf{R}}_j}], \\
\mathbf{z} = 1 & \quad \mu \sum_{j=1}^2 [(g_j + 2h_j) A_j^{(+)} e^{i\tilde{\mathbf{R}}} - (g_j - 2h_j) C_j^{(+)} e^{-i\tilde{\mathbf{R}}}] = \sum_{j=-}^+ j \tilde{n}_j [B_1^{(j)} e^{i\tilde{\mathbf{R}}_j} - B_2^{(j)} e^{-i\tilde{\mathbf{R}}_j}], \\
& \quad \mu \sum_{j=1}^2 [A_j^{(+)} e^{i\tilde{\mathbf{R}}} - C_j^{(+)} e^{-i\tilde{\mathbf{R}}}] = \sum_{j=-}^+ \tilde{n}_j [B_1^{(j)} e^{i\tilde{\mathbf{R}}_j} - B_2^{(j)} e^{-i\tilde{\mathbf{R}}_j}]. \\
\hline
\end{aligned}$$

TABLE III: Boundary conditions for TE waves corresponding to TWS slab. Here effective indices \tilde{n}_{\pm} are defined by (16), and functions g_j and h_j are given in (34).

- [12] S. -Y. Xu, I. Belopolski, N. Alidoust, M. Neupane, G. Bian, C. Zhang, R. Sankar, G. Chang, Z. Yuan, C. -C. Lee, S. -M. Huang, H. Zheng, J. Ma, D. S. Sanchez, B. Wang, A. Bansil, F. Chou, P. P. Shibayev, H. Lin, S. Jia, and M. Z. Hasan, *Science* **349**, 613 (2015).
- [13] B. Q. Lv, H. M. Weng, B. B. Fu, X. P. Wang, H. Miao, J. Ma, P. Richard, X. C. Huang, L. X. Zhao, G. F. Chen, Z. Fang, X. Dai, T. Qian, and H. Ding, *Phys. Rev. X* **5**, 031013 (2015).
- [14] J. Ruan, S. -K. Jian, H. Yao, H. Zhang, S. -C. Zhang, and D. Xing, *Nat. Commun.* **7**, 11136 (2016).
- [15] X. Huang, L. Zhao, Y. Long, P. Wang, D. Chen, Z. Yang, H. Liang, M. Xue, H. Weng, Z. Fang, X. Dai, and G. Chen, *Phys. Rev. X* **5**, 031023 (2015).
- [16] C. -L. Zhang et al., *Nat. Commun.* **7**, 10735 (2016).
- [17] B. Sviderski, G. Pohl, E. J. Bergholtz, and P. W. Brouwer, *Phys. Rev. Lett.* **113**, 026602 (2014).
- [18] P. Baireuther, J. M. Edge, I. C. Fulga, C. W. J. Beenakker, and J. Tworzydło, *Phys. Rev. B* **89**, 035410 (2014).
- [19] M. A. Naimark, *Trudy Moscov. Mat. Obsc.* **3**, 181 (1954) in Russian, English translation: *Amer. Math. Soc. Transl.* (2), **16**, 103 (1960).
- [20] G. Sh. Guseinov, *Pramana J. Phys.* **73**, 587 (2009).
- [21] A. Mostafazadeh, *Geometric Methods in Physics*, Trends in Mathematics, edited by P. Kielanowski, P. Bieliavsky, A. Odziejewicz, M. Schlichenmaier, and T. Voronov (Springer, Cham, 2015) pp 145-165; arXiv: 1412.0454.
- [22] A. Mostafazadeh, M. Sarisaman, *Phys. Lett. A* **375**, 3387 (2011); *Proc. R. Soc. Lond. Ser. A Math. Phys. Eng. Sci.* **468**, 3224 (2012); *Phys. Rev. A* **87**, 063834 (2013); *Phys. Rev. A* **88**, 033810 (2013); *Phys. Rev. A* **91**, 043804 (2015).
- [23] A. Mostafazadeh and M. Sarisaman, *Ann. Phys. (NY)* **375**, 265-287 (2016).
- [24] M. Sarisaman and M. Tas, *J. Opt. Soc. Am. B* **35**, 2423 (2018).
- [25] M. Sarisaman and M. Tas, *Ann. Phys. (NY)* **401**, 139-148 (2019).
- [26] A. Mostafazadeh, *Phys. Rev. A* **83**, 045801 (2011).
- [27] W. T. Silfvast, *Laser Fundamentals*, Cambridge University Press, Cambridge, 1996.
- [28] I. Kriegel, M. Guizzardi, F. Scotognella, *Ceramics* **1**(1), 139-144 (2018).
- [29] J. Buckeridge, D. Jevdokimovs, C. R. A. Catlow, and A. A. Sokol, *Phys. Rev. B* **93**, 125205 (2016).
- [30] B. J. Ramshaw, K. A. Modic, A. Shekhter, Y. Zhang, E. Kim, P. J. W. Moll, M. D. Bachmann, M. K. Chan, J. B. Betts, F. Balakirev, A. Migliori, N. J. Ghimire, E. D. Bauer, F. Ronning and R. D. McDonald, *Nature Comm.* **9**, 2217 (2018).
- [31] M. Dadsetani, A. Ebrahimi, *Journal of Elec. Mater.* **45**, 5867 (2016).
- [32] P. Hosur, S. A. Parameswaran and A. Vishwanath, *Phys. Rev. Lett.* **108**, 046602 (2012).
- [33] M. Kargarian, M. Randeria, and N. Trivedi, *Scientific Reports* **5**, 12683 (2015).
- [34] Y. D. Chong, L. Ge, H. Cao, and A. D. Stone, *Phys. Rev. Lett.* **105**, 053901 (2010).
- [35] S. Longhi, *Physics* **3**, 61 (2010).
- [36] S. Longhi, *Phys. Rev. A* **82**, 031801 (2010).
- [37] S. Longhi, *Phys. Rev. A* **83**, 055804 (2011).

- [38] S. Longhi, Phys. Rev. Lett. **107**, 033901 (2011).
- [39] W. Wan, Y. Chong, L. Ge, H. Noh, A. D. Stone, and H. Cao, Science **331**, 889 (2011).
- [40] L. Ge, Y. D. Chong, S. Rotter, H. E. Türeci, and A. D. Stone, Phys. Rev. A **84**, 023820 (2011).
- [41] D. G. Baranov, A. E. Krasnok, T. Shegai, A. Alù, and Y. D. Chong, Nature Reviews Materials **2**, 17064 (2017).
- [42] A. Mostafazadeh, Phys. Rev. Lett. **102**, 220402 (2009).
- [43] M. Sarisaman, Phys. Rev. A **95**, 013806 (2017).
- [44] M. Sarisaman and M. Tas, Phys. Rev. B **97**, 045409 (2018).
- [45] For the sake of full discussion, we keep its presence till the end.
- [46] Time harmonic electric field corresponds to $\vec{\mathcal{E}}(\vec{r}, t) := \vec{E}(\vec{r}) e^{-i\omega t}$, similarly for $\vec{\mathcal{B}}(\vec{r}, t)$, $\vec{\mathcal{D}}(\vec{r}, t)$ and $\vec{\mathcal{H}}(\vec{r}, t)$ fields.
- [47] We obtain the TE mode solution of the Kerr and Faraday rotated optical system by specifying $\vec{E} = E_x \hat{e}_x + E_y \hat{e}_y$, where $E_x(\vec{r}) = \mathcal{E}_x(z) e^{ik_x x}$ and $E_y(\vec{r}) = \mathcal{E}_y(z) e^{ik_x x}$.
- [48] Here we use superindex j to avoid abuse of notation in Eq. 17. \mathfrak{K}^j simply refers to the wavenumber corresponding to the mode j .